nature communications

Article

https://doi.org/10.1038/s41467-024-51799-4

Structural transition of GP64 triggered by a pH-sensitive multi-histidine switch

Received: 15 April 2024

Accepted: 16 August 2024

Jinliang Guo[1,4], Shangrong Li[1,4], Lisha Bai[2,4], Huimin Zhao[1,4], Wenyu Shang[1], Zhaojun Zhong[1], Tuerxunjiang Maimaiti[1], Xueyan Gao[1], Ning Ji[2], Yanjie Chao[3], Zhaofei Li[2] & Dijun Du[1]

The fusion of viruses with cellular membranes is a critical step in the life cycle of enveloped viruses. This process is facilitated by viral fusion proteins, many of which are conformationally pH-sensitive. The specifics of how changes in pH initiate this fusion have remained largely elusive. This study presents the cryo-electron microscopy (cryo-EM) structures of a prototype class III fusion protein, GP64, in its prefusion and early intermediate states, revealing the structural intermediates accompanying the membrane fusion process. The structures identify the involvement of a pH-sensitive switch, comprising H23, H245, and H304, in sensing the low pH that triggers the initial step of membrane fusion. The pH sensing role of this switch is corroborated by assays of cell-cell syncytium formation and dual dye-labeling. The findings demonstrate that coordination between multiple histidine residues acts as a pH sensor and activator. The involvement of a multi-histidine switch in viral fusion is applicable to fusogens of human-infecting thogotoviruses and other viruses, which could lead to strategies for developing anti-viral therapies and vaccines.

Enveloped viruses enter host cells by merging viral and cellular membranes, and fusion is usually mediated by glycoproteins on the viral surface[1,2]. Based on structural characteristics, three classes of viral fusion proteins (fusogens) have been identified[1,2]. In their postfusion state, class I proteins feature a trimeric coiled-coil structure at the N-terminus, which is flanked in the opposite direction by segments adjacent to the transmembrane domain, forming a hallmark 'six-helix bundle' structure[3]. Class II proteins transition from a β-sheet-rich dimer prefusion state to a trimer postfusion state[4]. Class III proteins exhibit features similar to those of both class I and II proteins, and are especially evident in their postfusion forms[5,6]. Generally, viral fusion proteins undergo conformational changes from a metastable prefusion state to a stable postfusion state during the fusion process. For different viruses, their fusogens employ diverse strategies to initiate the membrane fusion reaction[2], such as receptor binding in human immunodeficiency virus 1 (HIV-1)[7], pH changes in influenza and rhabdoviruses[5,6,8], or a mixture of both, as reported for avian sarcoma and leukosis virus (ASLV)[9]. Additionally, certain fusogens, such as glycoprotein S of severe acute respiratory syndrome coronavirus-1 (SARS-CoV-1) and SARS-CoV-2, utilize a protease-triggered fusion mechanism[10,11].

During entry into endosomes, certain class I, II, and III fusogens are activated at low pH between ~5.0 and 6.8[2]. Accumulating data from many viral fusion systems have demonstrated that electrostatic repulsion generated by protonation of histidines (pKa 6.04) and in some cases aspartates (pKa 3.9) and glutamates (pKa 4.25) controls pH-dependent conformational changes of viral fusogens[2,12]. In proposed models, at the prefusion state, the histidine residues of viral fusogens interact with other cationic residues (Lys, Arg, or His). As the environmental pH decreases, these histidine residues are protonated

---

[1]School of Life Science and Technology, ShanghaiTech University, Shanghai, China. [2]State Key Laboratory of Crop Stress Biology for Arid Areas, Key Laboratory of Plant Protection Resources and Pest Management of Ministry of Education, Key Laboratory of Integrated Pest Management on the Loess Plateau of Ministry of Agriculture and Rural Affairs, College of Plant Protection, Northwest A&F University, Yangling 712100 Shaanxi, China. [3]CAS Key Laboratory of Molecular Virology and Immunology, Shanghai Institute of Immunity and Infection, Chinese Academy of Sciences, Shanghai, China. [4]These authors contributed equally: Jinliang Guo, Shangrong Li, Lisha Bai, Huimin Zhao. e-mail: zhaofeili@nwsuaf.edu.cn; dudj@shanghaitech.edu.cn

and the interaction clusters repel, destabilizing the prefusion state and promoting the conformation transition[12,13]. Although recent studies demonstrate that histidine residues play critical roles in mediating membrane fusion in many viral fusion proteins, the defined roles of these charged residues in triggering pH-dependent conformation change remain largely elusive. In some cases, a single key histidine residue likely acts as a pH sensor[14,15]. In other instances, such as with influenza virus HA, multiple histidine residues (and other types of residues) might coordinate to sense low pH and initiate fusion-related structural transition[15–19].

Class III viral fusogens are found in diverse viral families including *Baculoviridae*, *Hepeviridae*, *Rhabdoviridae*, and *Orthomyxoviridae*[2,20]. Currently, the postfusion structures of this group have been solved for: (a) glycoprotein GP64 of the baculovirus Autographa californica multiple nucleopolyhedroviurs (AcMNPV)[21]; (b) glycoprotein B (gB) of herpesviruses, including that of Epstein-Barr virus (EBV)[22], herpes simplex virus type 1 (HSV-1)[23], and human cytomegalovirus (HCMV)[24]; (c) glycoprotein (G) of rhabdoviruses from Chandipura virus G (CHPV)[25], Mokola virus G (MOKV)[16], and vesicular stomatitis virus (VSV)[6]; and (d) glycoprotein (Gp) of thogotoviruses from Bourbon virus (BRBV)[26], Dhori virus (DHOV), and Thogoto virus (THOV)[27]. These data reveal that class III fusion proteins adopt a similar postfusion fold, although they share low sequence identities. Accumulating structural data from rhabdoviruses G that captured in prefusion and intermediate states[5,28,29] indicate that G proteins are stable and can reversibly transition between the trimeric prefusion and postfusion states via monomeric intermediates as the pH decreases, and vice versa[6,7,30,31]. The rhabdovirus G proteins are activated to facilitate membrane fusion within endosomes. Mutational analyses revealed that two histidine residues H389 and H407, and several glutamates residues (D268, D274, D393 and D395) may act as pH-sensitive switches during VSV-G conformational change[32,33]. Recently, the solved prefusion structures of HSV-1 and HCMV gBs[34–36] suggest that they are likely metastable and transition irreversibly from prefusion to postfusion states. Additionally, unlike rhabdoviruses G, the pH-sensitive switches are absent from both the prefusion and postfusion structures of gB[34]. HSV-1 fuses with a host cell at the plasma or endosomal membrane. The membrane fusion mediated by the HSV-1 gB relies on other viral envelope proteins gD, gH and gL[37].

As a prototype class III fusion protein, GP64 is the major envelope glycoprotein of AcMNPV, an archetypal member of the baculovirus family, which comprises large, enveloped DNA viruses of arthropods. AcMNPV serves as a powerful tool for protein expression, vaccine production, and mammalian cell transduction. GP64 is responsible for receptor binding and low pH-induced membrane fusion during virus entry[38–42]. In its postfusion state, GP64 is predominantly composed of β-sheets with a long central coiled coil[21], and displays high structural similarity to Gp of BRBV, DHOV, and THOV[26,27], which also engage in low pH-induced membrane fusion[27]. In ectodomain, AcMNPV GP64 contains 14 histidine residues. Most of them are highly conserved among GP64 homologs[39] and several histidines located at the trimer interface have been proposed to function as the pH-sensitive switch to trigger the conformational change[21]. Mutational analysis reveals that none of the individual histidine in the ectodomain of GP64 are necessary for low-pH triggered membrane fusion, but a cluster of histidines (H245/H304/H430) in the vicinity of domain II, the tip of central helix, and the C-terminal part of the ectodomain is critical for the stability of prefusion conformation and fusion[39]. For lack of the prefusion structure, the coordination of other histidine residues in regulating low-pH triggered conformational change of GP64 is not clear.

In this work, we determine GP64 structures in prefusion and early intermediate states using cryo-EM. Comparison of prefusion, early intermediate and postfusion structures reveals structural rearrangements accompanying the membrane fusion process. The structures together with the results of accompanying biochemical analyses identify a pH-sensitive switch, comprising H23, H245, and H304, involved in sensing the low pH that triggers the initial step of membrane fusion. The viral fusion mechanism is applicable to fusogens of human-infecting thogotoviruses and many other viruses.

Results

Cryo-EM structure determination and overall structure

Due to its metastability, prefusion GP64 is difficult to purify for structural analysis. To overcome this challenge, the native GP64 protein was isolated from the plasma membrane of recombinant baculovirus-infected Sf9 cells using the mild detergent *n*-dodecyl-*β*-D-maltoside (DDM) and purified without an affinity purification tag. To improve stability, the protein was reconstituted into Saposin A lipid nanodiscs[31,43,44].

The structure of GP64 was solved using single-particle cryo-EM. Images of the same preparation were subjected to classification and 3D variability analyses, revealing different conformational states. Two density maps were reconstituted from the particle subsets: (a) GP64 map-1 at 2.77 Å resolution showing 3-fold symmetry; (b) GP64 map-2 at 2.97 Å resolution showing an asymmetric arrangement. With dimensions of 125 Å × 80 Å for the ectodomain, compared with 150 Å × 55 Å for the postfusion structure[21], the 3-fold symmetrical GP64 structure was in the prefusion state, and the asymmetric structure appeared to be in an early intermediate state (Supplementary Fig. 1a–j; Supplementary Fig. 2a; Supplementary Fig. 3a, b). The quality of both maps was excellent, allowing to construct models of prefusion and early intermediate states for residues 23–487 without gap (Supplementary Fig. 2a). Additionally, there was clear density for the starting residues of four oligosaccharide chains at N197, N354, N384, and N426, which are important for the binding of budded viruses to cells (Supplementary Fig. 2b)[45].

GP64 comprises seven domains (nomenclature defined in Fig. 1a and Supplementary Fig. 4). Domains I to V are in the ectodomain, followed by the pre-transmembrane domain (PTMD) and the transmembrane domain (TMD). The central core of the protein consists of domain III, helix D of domain V, the PTMD, and the TMD, all positioned at the trimer interface, centered around the 3-fold axis, and aligned from the N- to the C-terminus toward the center of the virion. Domains I, II, and IV are situated on the periphery of the molecule (Fig. 1b, c). The GP64 trimer adopts a tripod-like structure. The fusion domain (domain I) in each tripod leg comprises two fusion loops at the tips[46]. Like in the postfusion structure, the ectodomain contains seven disulfide bridges (Supplementary Fig. 4)[21,47].

Prefusion state structure of GP64

In the prefusion GP64, domains I to IV retained similar overall folds to those in the postfusion state. However, the arrangement of these domains in the prefusion state differed significantly from that in the postfusion state (Fig. 1b, c and Supplementary Fig. 5a, b). Domains I/II on the peripheral side of the molecule are linked to helix B of domain III through the basic loop (BL) segment spanning residues 271–297. This loop creates a folded structure on the surface by forming salt bridges and hydrogen bonds with neighboring protomers. These interactions help to maintain the molecule in its prefusion state (Fig. 2a). The BL structure explains the conformational recognition of GP64 by antibodies, such as the monoclonal antibody (MAb) AcV1, which recognizes the prefusion state of GP64 but not the postfusion conformation[48]. The AcV1 epitope is located on a segment of BL (residues 271–294) (Supplementary Fig. 6), which is ordered in the prefusion conformation but disordered in the postfusion state, suggesting that folding is required for recognition. The antibody AcV5 is not conformation-specific and binds both states[49]. The AcV5 epitope maps to residues 431–439, which are partially exposed in both prefusion and postfusion states (Supplementary Fig. 6).

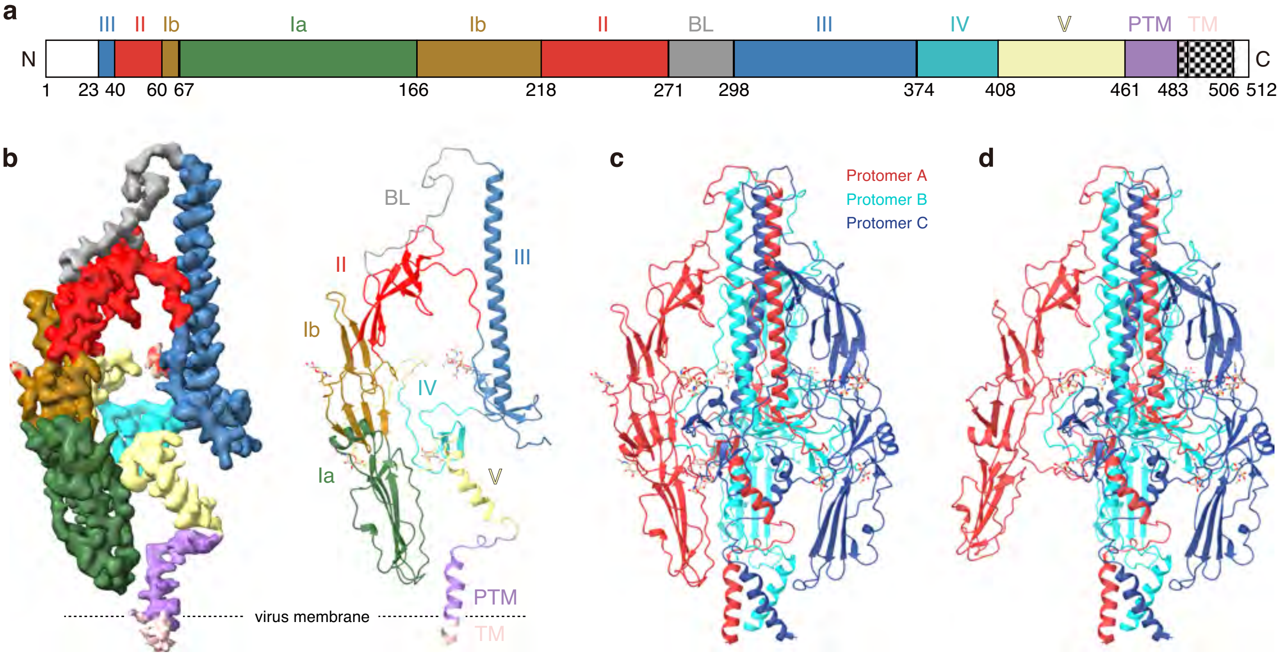

Fig. 1 | Overall structures of GP64 in prefusion and early intermediate states. **a** Linear representation of GP64 (the color code in (**a**) is also used for domains and subdomains in (**b**)). The signal peptide (residues 1–20), part of domain III (residues 21 and 22), and the C-terminal region (residues 488–512) are not observed in the structure and are colored white. The transmembrane region (TM) is labeled using a checkerboard pattern. **b** Density map (left) and ribbon diagram (right) of a prefusion GP64 monomer. **c** Ribbon diagram of a GP64 trimer in the prefusion state. Protomers A, B, and C are colored red, cyan, and dark blue, respectively. **d** Ribbon diagram of GP64 in the intermediate state; the coloring scheme is the same as in (**c**). Protomer A adopts an early intermediate state, while protomers B and C are almost in the prefusion conformation.

As BL spans the upper portion of the molecule, domain III relocates to the opposite side, positioning helix B of domain III adjacent to domain II of protomer C (Fig. 1c and Fig. 2a). In the trimer configuration, the B helices create a triple-stranded coiled-coil, establishing extensive interactions (Fig. 1c). The length of the B helices is consistent with the postfusion structure, unlike the central coiled-coil in VSV-G, a counterpart of domain III, which extends during its structural transition[5,6]. Domain IV has a defined structure, with residues 386–395 forming two antiparallel β-sheets. Like in the postfusion structure, helix C and the β-sheets in domain III, along with domain IV, are predominantly enveloped by the adjacent protomers, leading to robust interactions. Hence, dissociation of domains III and IV is unfavorable during rearrangement, which is in contrast to the transitions observed for VSV-G[5,6].

Residues 23–50, named conformation transform segment 1 (CTS1), are mostly engaged in the grooves between the B helices of protomers A and B, forming a pseudo ‘six-helix bundle’ structure (Fig. 1c and Supplementary Fig. 5c). CTS1 interacts with the B helices of protomers A and B; the β-sheet in domain III of protomer B; the β-sheet in domain I of protomer C; and a fragment from domain V (residues 409-429) of protomer C. Residues L38 of CTS1 form hydrogen bonds with N331 and H335, and T41 and K44 form hydrogen bonds with H326 and N319 in the adjacent protomer, respectively (Supplementary Fig. 5c).

In the prefusion GP64 arrangement, domain I interacts with a portion of domain IV (residues 372–385) in protomer C. K140 in protomer A forms a hydrogen bond with H378 in protomer C. A section of domain II (residues 218–271) engages with the initial part of helix B in protomer B, with much less contact than in the postfusion state (Fig. 2b).

A curled segment spanning residues 408–436 in domain V, designated conformation transform segment 2 (CTS2), is mostly sandwiched between domains I and II of its protomer and the beginning of CTS1 of protomer B, establishing extensive contacts (Fig. 1b, c).

The D helix of domain V is bent and intertwines with the adjacent protomers to form a trimer. Residue K434 forms a salt bridge with E454 of the adjacent protomer. Residue W439 packs against its counterparts in adjacent protomers to stabilize the prefusion structure (Fig. 2c)[50]. Domains I and II have no contact with adjacent protomers, and domain I has no contact with helix D. These interactions differ substantially from those of the postfusion configuration[21].

The initial coils of PTMDs also intertwine in a trimeric structure with those of adjacent protomers. The subsequent helix E in PTMD together with the TMD (helix F) forms an almost straight structure. The hydrophilic PTMD rises above the lipid bilayer, while the hydrophobic TMD integrates further into the viral envelope (Fig. 2d). These PTMD-TMD helices intersect at an angle of ~58°, with contacts at the central region through residue K479, and both the N- and C-termini spread apart. Fusion loop 1 (FL1) is anchored to the PTMD. This differs from herpesvirus gB, in which the amphipathic membrane-proximal region (MPR) forms a ‘scabbard’ at the membrane surface to shield FLs[34,37]. Two hydrophobic amino acids (L476 and L480) in PTMD interact with residue L82 in FL1 (Fig. 2e). These residues are involved in membrane fusion activity and the formation of fusion pores[21,51]. The specific features and amino acid sequences, particularly the length of the hydrophobic TMD, play important roles in membrane anchoring, membrane fusion, and virus budding[52].

Intermediate state structures of GP64

In the intermediate state structure of GP64, the two protomers retain their characteristics in the prefusion state. However, in the third protomer, domain I rotates ~40° around the hinge between domains I and II, forcing it away from the β-sheets of domains III and IV in protomer C (Fig. 1d). This protomer is identified as protomer-M. A GP64 trimer consisting of one protomer-M and two protomers in a conformation similar to prefusion GP64 is referred to as being in its intermediate-M state, which represents an early intermediate state. The conformations of domains I and II in protomer-M are similar to those in the postfusion

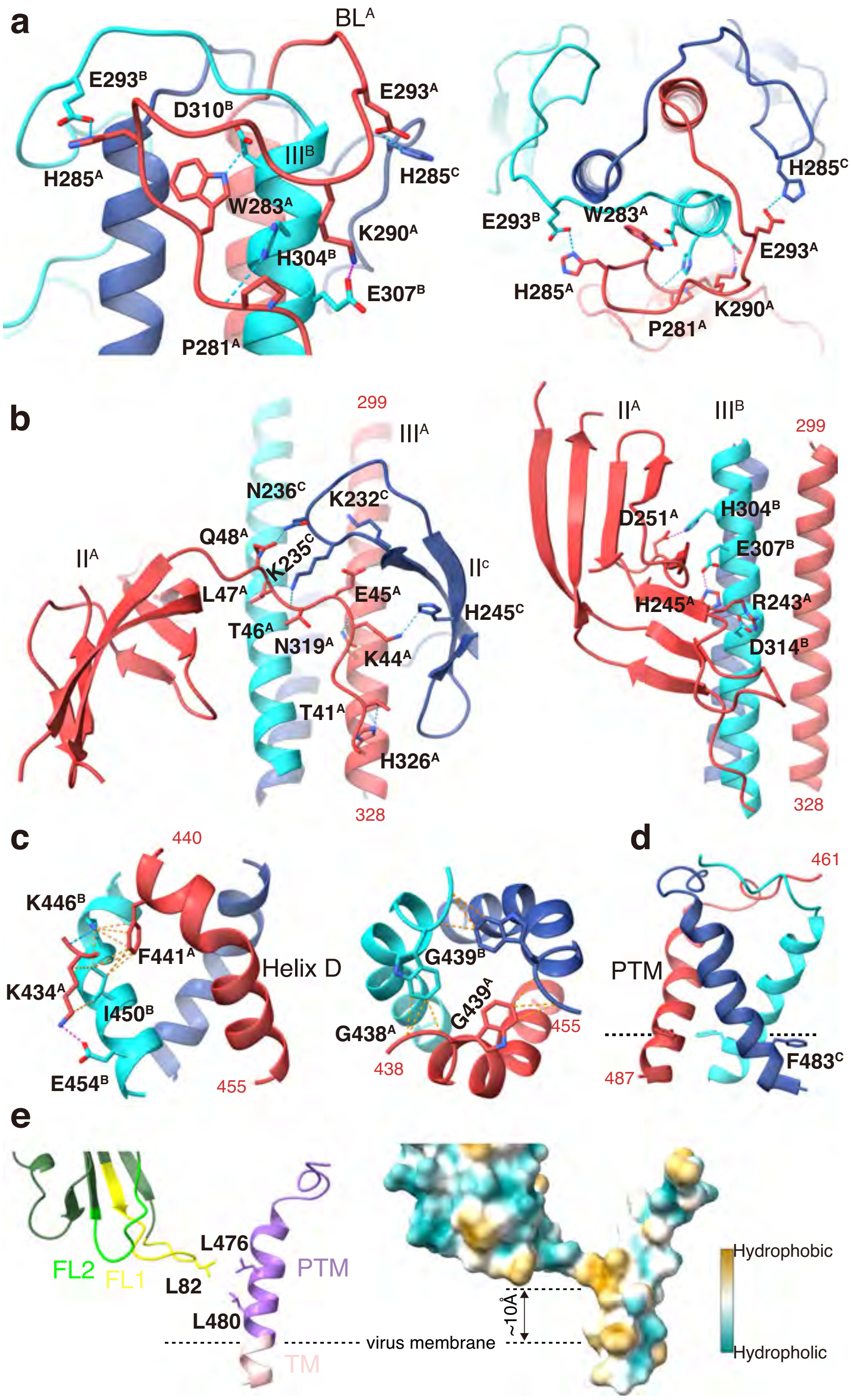

Fig. 2 | Structural details of prefusion GP64. Domains and subdomains in (**a**–**d**) are color-coded as in Fig. 1c. Superscripts A, B, and C on labels indicate protomers A, B, and C, respectively. Salt bridges, hydrogen bonds, and van der Waals contacts are indicated by dotted magenta, cyan, and dark orange lines respectively. **a** Side and top views showing intra- and interprotomer interactions between the basic loop (BL) of protomer A and the BLs/B helices of adjacent protomers. BL forms a stable structure through these interactions. **b** Interactions between domains II and III in prefusion (left) and postfusion[21] (right) (PDB code: 3DUZ) states. **c** Ribbon representation of the helix D trimer in the prefusion state viewed parallel to the membrane (left) and perpendicular to the membrane (right). **d** Ribbon representation of PTMD and TMD trimers of prefusion GP64. **e** Ribbon (left) and surface (right) representations of domain I, PTMD, and TMD showing interactions between fusion loop-1 and PTMD. Fusion loops are ~10 Å above the viral envelope membrane. Residues are colored as in Fig. 1a (left), or based on hydrophobicity (right).

structure of GP64. During the transformation, domains I and II disengage from the central core of the protein, while the linkers between domain II and BL/CTS1 remain rigid, as in the prefusion state.

The structure of DHOV-Gp was recently solved in an intermediate state (Accession code: 7XYM). All three protomers of DHOV-Gp exhibited similar conformations to those of the protomer-M of GP64 (Supplementary Fig. 7a). This DHOV-Gp trimer is referred to as being in its intermediate-T state. A model of the GP64 intermediate-T state was derived based on its protomer-M and DHOV-Gp intermediate-T state structures (Supplementary Fig. 7b). Until the intermediate-T state, domains III, IV, and V, as well as PTMD and TMD, exhibited little conformational change (Supplementary Fig. 7a, b).

Structural rearrangements during membrane fusion

Prefusion, intermediate, and postfusion structures of GP64 exhibit significant molecular rearrangement during conformational switching. Domains III and IV overall show little conformational change (Supplementary Fig. 5a), while the remaining parts of the molecule flip to the opposite end (Fig. 3a–c).

The conformational changes may involve a series of intermediate states. First, domain I rotates ~ 40° around the hinge between domains I and II, which disrupts the contacts between domains I/II and III/IV, as well as between the fusion loops and PTMD. Domains I/II remain rigidly linked to BL/CTS1. The shielded fragment of CTS2 is exposed to the solvent (Fig. 3a, b and Supplementary Fig. 7b).

The subsequent Intermediate states were predicted based on prefusion, intermediate, and postfusion GP64 structures, and other class III fusion proteins[34,53]. Unfolding of BL and disengagement of CTS1 from the groove between the B helices of protomers A and B allowed domain I and II to flip together following a ~ 180° rotation around the linkers between domain II and BL/CTS1, and then clip toward the molecular 3-fold axis, which orients domain I toward the host membrane (Fig. 3c). In this extended intermediate, the Ia domains establish contacts at the trimer interface via fusion loops FL1 and FL2. Domain II is snugly positioned against helix B of protomer B but in the reverse direction.

Finally, the curled CTS2 of protomer C straightens and engages in the groove between the B helices previously taken by CTS1. In the trimer configuration, this feature is reminiscent of the 'six-helix bundle' structure present in the postfusion form of class I fusion proteins[3]. The intertwined D helices and PTMD/TMD domains in the prefusion and intermediate-M/T states must be untwined. Residues on CTS2 form salt bridges with the histidine and aspartic acid residues on the B helices, which drive the foldback of the extended intermediate[54], prompting helix D to ascend next to domains I and II, positioning both PTMD and TMD, to which it is connected, at the same end of the molecule (Fig. 3c, d).

Throughout this structural transition, domains I, II, V, PTMD, and TMD move ~ 180° from one end of the molecule to the opposite end. Within the trimer, these movements are the result of coordinated adjustments of specific molecular regions.

Key histidines control pH-dependent conformational changes

GP64 undergoes a low pH-triggered conformational switch that may be facilitated by histidine residues[39]. GP64 contains 14 histidines in the ectodomain. In the prefusion structure, five histidines within FL2 (H152, H155, and H156), domain II (H205) and BL (H274) form contacts with the adjacent residues of the same protomer, while H324 and H430 at the trimer interface do not form contacts. The other seven histidines cluster as three groups at the trimer interface, mediating contacts with residues of adjacent protomers. The top group (H285 and H304) is situated between BL and the beginning segment of helix B. The middle group (H245, H326, and H335) plays a role in interactions between CTS1 and domain II/helix B, while the lower group (H23 and H378) mediates interactions between domains I and IV or the initial part of CTS1. In this configuration, the neutral H245 and H378 are positioned near the positively charged K44 and K140, respectively, forming hydrogen bonds. H285 and H304 engage in hydrogen bonds with E293 and P281, respectively; H23 forms hydrogen bonds with Y68 and E143; and H326 and H335 engage in hydrogen bonds with T41 and L38, respectively (Fig. 4a, left panel). In comparison to the prefusion state of GP64, the intermediate-M state reveals that residues in the Ia subdomain of protomer-M lose their contacts with H23 and H378 in the adjacent protomers. However, the interactions between the other histidines (H245, H285, H304, H324, H326, and H335) and their neighboring residues remain unchanged (Supplementary Fig. 8). In the postfusion structure, H274 and H285 are absent in the unsolved region, while interactions between H152, H155, H156, and H205 and adjacent residues are maintained or slightly altered. By contrast, contacts mediated by the other eight histidines are drastically changed due to structural rearrangement. Among them, H23 and H378 are released from their contacts in the prefusion state and remain free of contact, while the others (H245, H304, H324, H326, H335, and H430) form hydrogen bonds and/or salt bridges mainly with anionic residues (Asp or Glu) in close proximity (Fig. 4a, right panel), suggesting these histidines may participate in regulating the low pH-triggered conformational change.

As none of the individual histidines of GP64 play a dominant role in membrane fusion, based on previous studies[39], histidine residues at the trimer interface of prefusion GP64 (H23, H245, H285, H304, H324, H326, H335, and H378) were substituted with alanine in different combinations (Fig. 4b and Supplementary Table 1) to evaluate their roles in low pH-triggered conformational changes. In transiently expressing Sf9 cells, mutation of these histidines did not alter expression of the GP64 monomer (Fig. 4c). GP64 mutants containing double or multiple replacements of H23, H245, H285, H304, and H378 formed trimers (trimer I and trimer II) comparable with those typically observed for wild-type (WT) GP64, and the mutations had no significant effect on their cell surface level; however, trimerization and cell surface levels were significantly reduced for mutants H324/335 A and H326/335 A, and for mutants combining these replacements with other histidines (Fig. 4c, Supplementary Fig. 9 and Supplementary Table 1). Together with the low level of trimers for H326A and H324/326A in prior studies[39], these results suggest that H324, H326, and H335 are required to maintain the stability of GP64 trimers.

Cell-cell syncytium formation assays indicated that substitution of H23/H245 or incorporation of H23/245 A or H245/304 A mutations into other substitutions resulted in a dramatic reduction (70-80%) of the fusion activity. Intriguingly, substitution of H23/H245/H304 almost abolished the fusion activity of the modified GP64. Many other mutants with different combinations of histidine residues maintained WT levels or caused a minor reduction in fusion (Fig. 5a and Supplementary Table 1). Furthermore, dual dye-labeling assays showed that H23/245/304 A and H23/245/304/378 A induced low (~5%) transfers of a membrane dye (R18) and a cytosolic dye (calcein-AM) between labeled red blood cells (RBCs) and Sf9 cells. For H23/245 A and other constructs containing H23/245 A or H245/304 A mutations, 20–30% dye transfer was detected for both membrane and cytosolic dyes (Fig. 5b and Supplementary Table 1). These results are consistent with the low level of syncytium formation, and suggest that H23, H245, and H304 are essential for sensing low pH to trigger the initial step of membrane merging.

To further investigate whether the observed defect in membrane fusion was due to an impact on the conformational change triggered by low pH in the modified GP64s, which were present on the cell surface at levels comparable with the WT protein, the binding activity of monoclonal antibody AcV1 at the cell surface was assessed from pH 4.5 to 7.0. Upon decreasing the pH, significant loss of AcV1 binding was observed for WT GP64. Approximately 40–80% (H23/245 A, H23/245/378 A, and H245/304/378 A) or >95% (H23/245/304 A and H23/245/304/378 A) of the AcV1-binding efficiency was lost at neutral pH (Fig. 5c). Loss of AcV1 binding at various low pH conditions for constructs H23/245 A and H23/245/378 A was generally similar to and paralleled that of the WT protein. However, for H245/304/378 A, the AcV1-binding activity remained low level at pH 5.5–7.0, and then reduced slightly with the pH decreasing. Due to the low levels detected, AcV1 binding for H23/245/304 A and H23/245/304/378 A fluctuated upon decreasing low pH treatments. Similar to these constructs, two others with modified GP64s, K434A, and I450A/E454A, which retained the

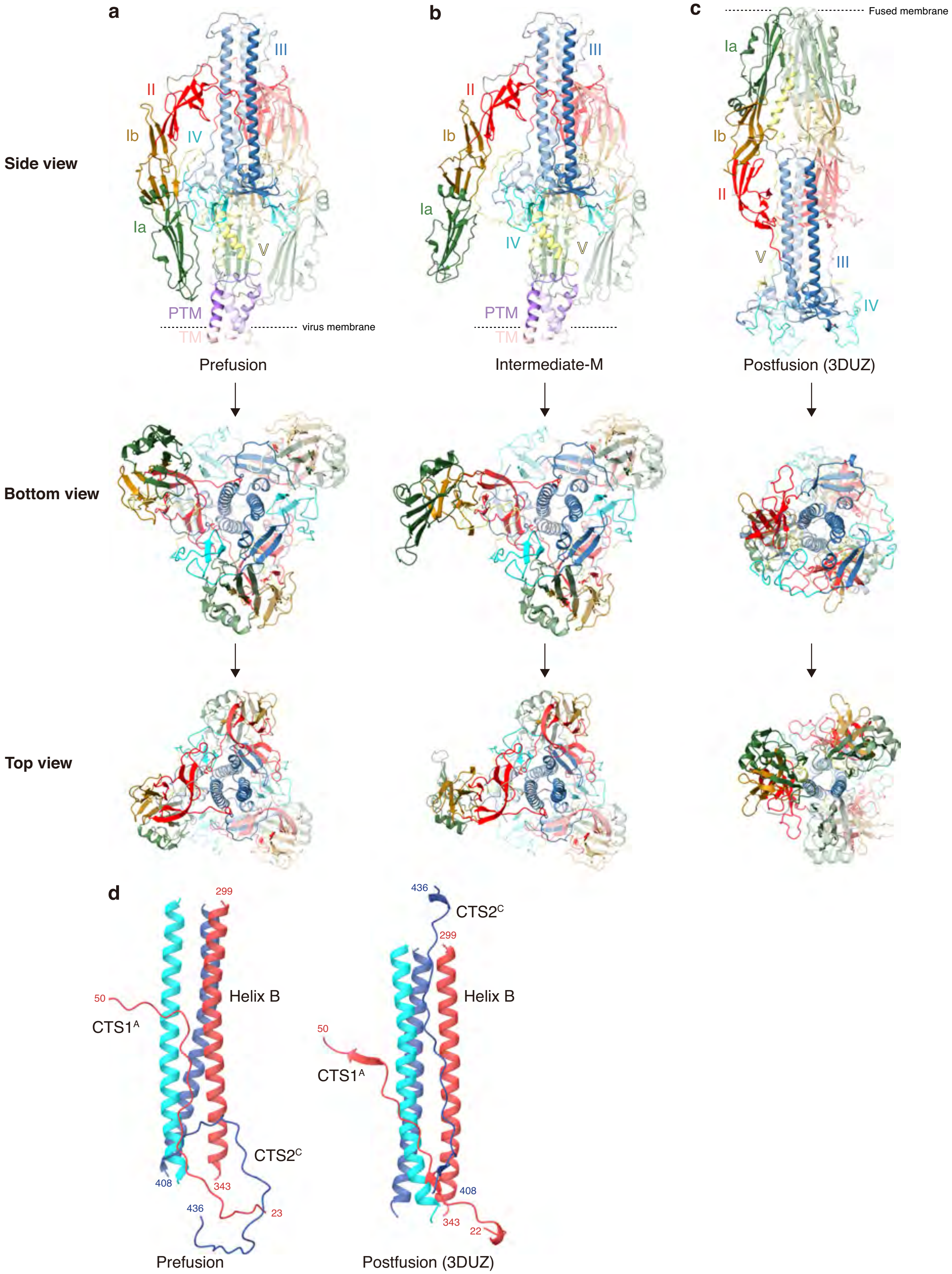

Fig. 3 | Structural rearrangements of GP64 during membrane fusion. a–c Side, bottom, and top views of GP64 in prefusion (**a**), intermediate-M (**b**), and postfusion[21] (**c**) states showing protein conformational changes. The coloring scheme is the same as that in Fig. 1a. For clarity, the C-terminal region (residues 437–487) is omitted in the bottom and top views of GP64. **d** Comparison of CTS1 and CTS2 in prefusion (left) and postfusion (right) states. The coloring scheme is the same as that in Fig. 1c. Superscripts A, B, and C on labels indicate protomers A, B, and C, respectively.

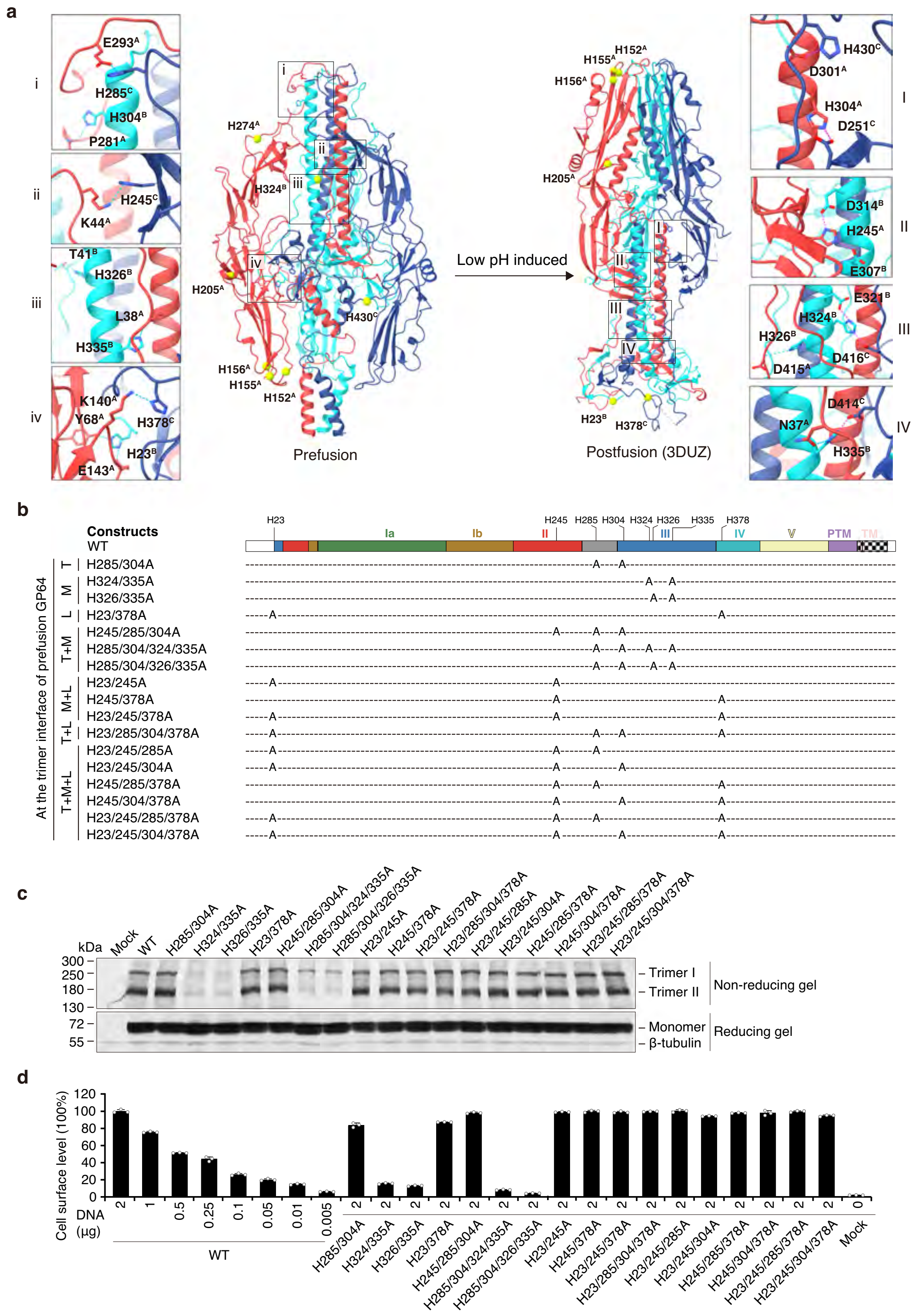

Fig. 4 | Construction and expression of His-to-Ala substituted GP64s. a pH-sensitive interfaces of GP64. Three clusters of histidine residues in the prefusion state are shown in regions indicated by black rectangles (left). The same residues are shown in the postfusion state[21] (right). Salt bridges and hydrogen bonds are indicated by dotted magenta and cyan lines. **b** Schematic diagram of GP64 constructs. T, M, and L represent top, middle, and lower regions, respectively, within the trimer interface of prefusion GP64. **c** Western blotting analysis of transient expression and trimerization of WT and modified GP64s. β-tubulin served as a loading control. **d** Relative cell surface levels of GP64s were measured via cELISA. A standard curve was generated by transfecting cells with decreasing quantities of a plasmid expressing WT GP64, which is shown on the left side of the panel. Error bars represent standard deviation (SD) from the mean of independent replicates ($n = 3$).

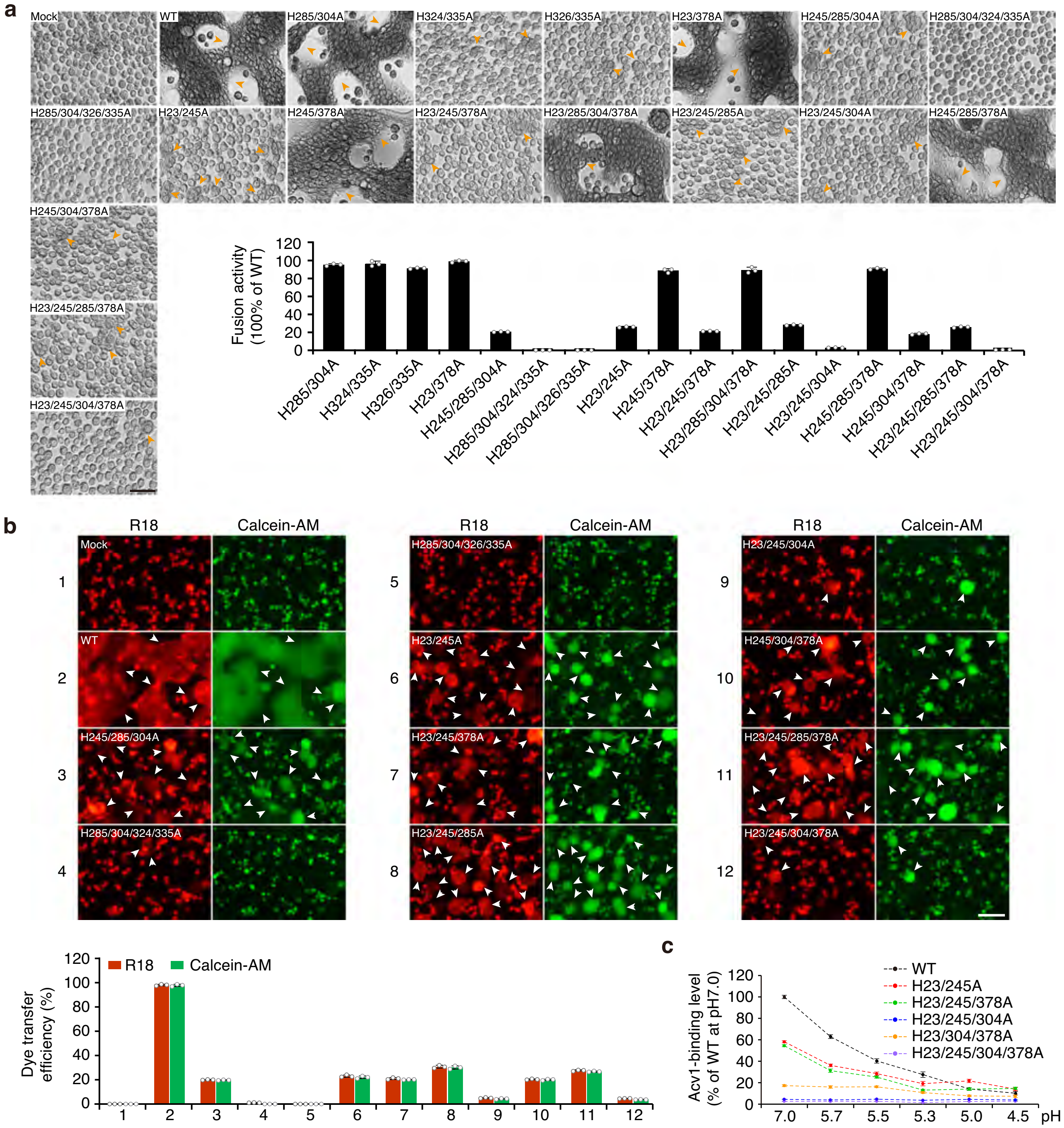

Fig. 5 | Membrane fusion and low pH-induced conformational changes in GP64s. a Cell-cell syncytium formation assay. At 36 h p.t., transfected cells were exposed to low pH to induce syncytium formation and fusion activity was measured. Arrows indicate the syncytial mass (≥5 nuclei). Error bars represent the SD from the mean of independent replicates ($n = 3$). **b** Hemifusion and pore formation mediated by fusion-deficient GP64s. The top panel shows hemifusion and pore formation mediated by the modified GP64s. The bottom panel shows dye transfer efficiency. The dye transfer efficiency was estimated as the ratio of the number of R18-transferred or calcein-AM-transferred Sf9 cells to the number of Sf9 cells with bound RBCs. Error bars represent the SD of means of independent replicates ($n = 3$). **c** Analysis of low pH-triggered conformational changes in fusion-deficient GP64 constructs. At 36 h p.t., the cell-surface-localized GP64 proteins subjected to low pH triggering were measured by cELISA using MAb AcV1 and then normalized against WT at pH 7.0. Error bars represent the SD from the mean of independent replicates ($n = 3$). Scale bar, 50 µm.

cell surface level of WT GP64 but exhibited low membrane fusion efficiency (1–2%), lost AcV1 binding under neutral and low pH conditions (Supplementary Fig. 9, Supplementary Fig. 10 and Supplementary Table 1). These results suggest that H23, H245, and H304, and the interaction network formed by K434, I450, and E454 at the bottom region of the trimer interface, are critical for stabilizing the conformation of GP64 at neutral pH.

In addition to mediating membrane fusion, GP64 is also required for virus binding and release[38–40]. Transfection-infection assays indicated that modified GP64 with lower fusion activity (<10%) could not efficiently rescue or completely abolish virus infectivity. Notably, for the H23/245 A construct, which exhibited significantly reduced fusion activity (~20%), virus infectivity was only slightly lower (~4-fold) than that of WT GP64. Incorporation of this mutation into H304A or H304/

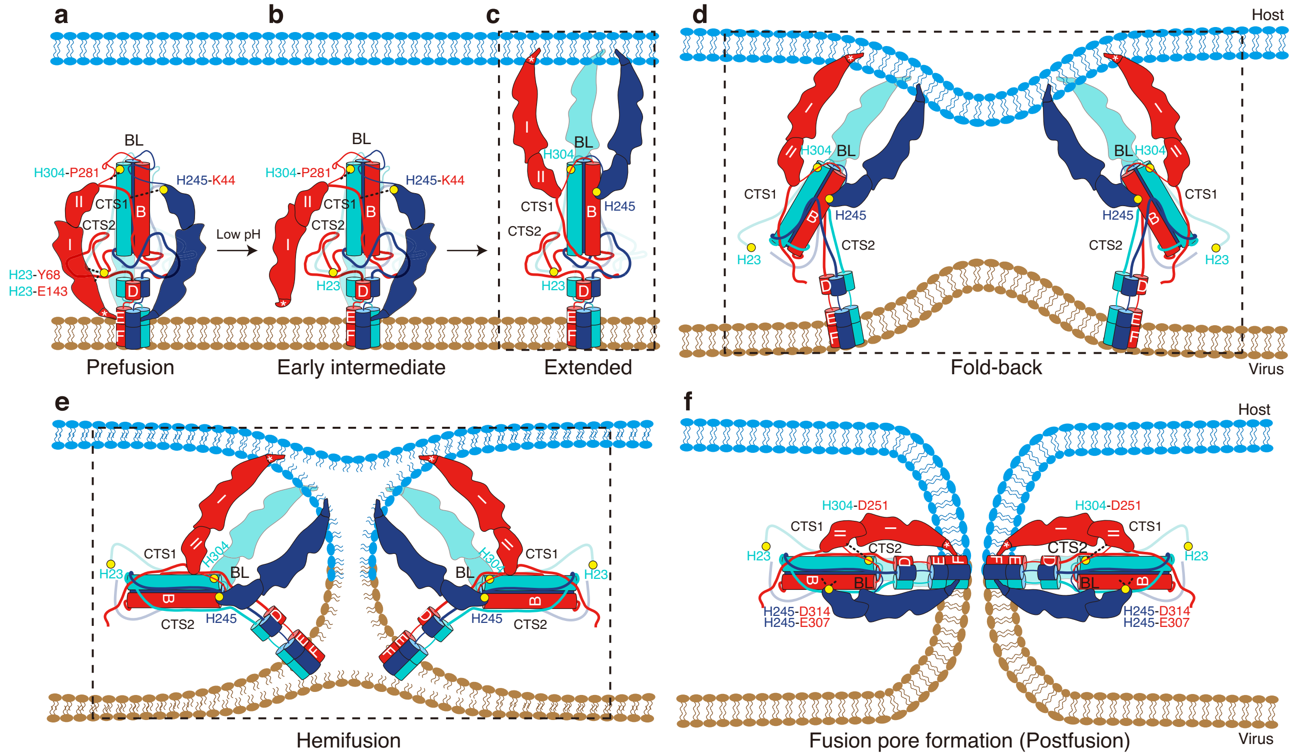

Fig. 6 | Schematic cartoon diagrams of GP64 rearrangements. a In the prefusion state (at neutral pH), domain I aligns with the β-sheets of domain IV and PTMD, while domain II aligns with the initial part of helix B of domain III. The fusion loops located at the tips of domain I are initially anchored onto PTMD. CTS1 of each protomer fits into the groove of the central helices. CTS2 forms a curled structure positioned between domains I/II and the central domains (III and IV). **b** During the transformation, rotation of domain I causes the disengagement of domains I/II from domains III/IV and the fusion loops from PTMD. This repositioning renders CTS2 accessible (This might indicate an early intermediate state). **c** Subsequently, domains I and II detach from the central core and rotate by 180°, and domain II aligns with the central helix again but in a reverse manner. The fusion loops attach to the host membrane. **d** CTS1 moves away from the grooves of the central helices, allowing CTS2 to straighten and snugly fit into this groove, driving foldback of the extended intermediate. **e**, **f** This action prompts helix D to ascend alongside domains I and II, positioning both PTMD and TMD, to which it is connected, at the same end of the molecule, causing the fusion of virus and host membranes. **c**–**e** depict later intermediate states, while (**f**) represents the postfusion state. The yellow dots represent the approximate locations of the key histidines H23, H245, and H304, respectively; while the black dashed lines indicate the interactions between these histidines and adjacent residues.

378 A severely impaired membrane fusion, and no infectious viruses were detected for those constructs (Supplementary Table 1). Further growth curve analysis suggested that the low infectivity of certain constructs may have resulted from lower rates of virion production and/or low virion infectivity (Supplementary Fig. 11). Taken together, these results suggest that H23/H245/H304 coordinate to control the low pH-triggered initial conformational transition of GP64.

Discussion

Enveloped viruses utilize a fusion protein or fusion complex to penetrate host cells. Some viruses employ pH-induced membrane fusion during viral entry, but the exact triggering mechanism involved remains largely unclear. In the current study, we tackled this problem through both structural and biochemical approaches, using the prototype GP64 of baculovirus as a model fusion protein.

By solving the structures of GP64 in its prefusion and early intermediate states, alongside the postfusion structure[21], we were able to determine the structural rearrangements that occur during the membrane fusion process. The results of structural and biochemical analyses indicated that coordination of histidines at the trimer interface of prefusion GP64, specifically H23, H245, H285, H304, H324, H326, H335, H378, and H430, plays a crucial role in either maintaining trimer stability or facilitating protein structural transformations. Notably, altering H326 or both H324 and H326, along with H335, significantly decreases trimer formation, underscoring their importance in trimer assembly and stability. By contrast, changes in H23/H245 or H245/H304, or combining these changes with mutations including H285A, H378A, or H430A, dramatically affect the prefusion conformation and fusogenicity of the protein, particularly in combinations such as H23/H245/H304 and H245/H304/H430[39]. Throughout the structural transition, the interactions mediated by these histidines are significantly altered: (a) H23 and H378 transition from interacting with adjacent protomer residues in the prefusion state to being free in the postfusion state; (b) H245 and H304 maintain interactions through the prefusion to early intermediate states, and thereafter engage with different residues (D314 and E307 for H245, D251 for H304) of the adjacent protomer in the postfusion state; (c) H430, initially free in the prefusion structure, forms a salt bridge with D301 from an adjacent protomer in the postfusion state. These results suggest that, alongside H245/H304, H430 might be crucial for the stability of the intermediate and/or postfusion structures of GP64, while H23, H245, and H304 predominantly respond to low pH, directing initial conformational changes of GP64.

Drawing on combined insights from structural and biochemical analyses, we developed a theoretical model to illustrate the conformational transformations of GP64 induced by low pH (Fig. 6). In an acidic environment, protonation of histidine residues leads to electrostatic repulsion between H378 and its neighboring K140, and disrupts the interaction between H23 and Y68/E143. These disruptions might initiate the conformational change and collectively induce a rotation of domain I, exposing a segment of CTS2 that was previously shielded (Fig. 6b). Throughout these intermediate-M/T states, domains I/II continue to be rigidly engaged with domain III, facilitated by the BL and CTS1 linkages. Subsequently, loss of interaction between H285/H304 and neighboring residues might lead to the unfolding of BL. In addition, loss of interaction between H245/H326/H335 and neighboring residues might enable CTS1 to detach from the grooves between the B helices. These changes relax the linkers between domains I/II and BL/CTS1, facilitating an ~ 180° rotation of domains I/II into an extended position. As a result, H245 and D251 in domain II form salt bridges with helix B of the adjacent protomer (H245 with E307 and D314; D251 with H304), positioning them in the reverse direction (Fig. 6c). In the final stage, the previously curled CTS2 straightens and engages in the groove between the B helices, a position originally occupied by CTS1. D414, D416, and H430 on CTS2 establish salt bridges with residues on helix B (D414 with H335; D416 with H324; H430 with D301), promoting foldback of the extended intermediate and the postfusion state transition, which ultimately facilitate the fusion of viral and host membranes (Fig. 6d–f).

The human-infecting thogotovirus glycoproteins display high structural similarity to GP64 in the intermediate and postfusion states, and engage in low pH-induced membrane fusion (Supplementary Fig. 7a and Supplementary Fig. 12)[27]. The involvement of a multi-histidine switch in viral fusion is likely applicable to fusogens of thogotoviruses and other viruses. Understanding the exact process through which low pH induces structural alterations in GP64 requires further structural and functional studies. Insights into the fusion of GP64-mediated viruses with the host cellular membrane could lead to strategies for antiviral intervention and vaccine development against human pathogens.

The relatively high pH in early endosomes of mammalian cells decreases the fusogenicity of GP64, which in turn reduces the transduction efficiency of the virus and limits its application as a vector for gene therapy[55]. Understanding how GP64-mediated viruses merge with the host cell membrane could help to change the fusogenicity of GP64 to broaden the host range of the virus, which would improve its mammalian cell transduction efficiency.

Methods

Mutagenesis and construction of plasmids and bacmids

The 5′-end 833 bp and 3′-end 706 bp fragments of the AcMNPV *gp64* open reading frame (ORF) containing alanine-substituted mutations were synthesized and inserted into the XbaI and NotI, or NotI and EcoRI sites of pBieGP64[52] or Myc-GP64pBlue[50] to generate the transient expression plasmid Pie1-XpBlue or Pie1-Myc-YpBlue (X and Y represent a specific modified GP64). Next, fragments encoding WT or substituted GP64 were isolated from pBieGP64, Pie1-XpBlue, or Pie1-Myc-YpBlue using XbaI and EcoRI restriction enzymes, and separately inserted into Pgp64-GFPpFB, which generated by replacement of the promoter and ORF of GP64 in GP64pFB[52] with a fused fragment containing the promoter of AcMNPV *gp64* and the ORF of GFP, to generate the pFastBac plasmids Pgp64-XpFB and Pgp64-Myc-YpFB. A synthesized fragment of choline transporter-like protein 2 (CTL2; UniProt ID: Q8IWA5) containing a 10 × His-tag at its C-terminus was inserted into the BamHI and EcoRI sites of pFastBac1 to generate pFastBac-CTL2. The resulting pFastBac constructs were each cloned and inserted into the *polyhedrin* locus of an AcMNPV bacmid (bMON14272 for CTL2) or a *gp64*-null bacmid[52] (for WT or modified GP64) by Tn7-mediated transposition. Transfection of Sf9 cells was performed using X-tremeGENE 9 DNA Transfection Reagent (6365779001; Roche) or using the $CaPO_4$ precipitation method[52].

Purification of Saposin A and nanodisc reconstitution

A synthesized fragment of the coding sequence for human Saposin A was inserted into the pET15b vector. pET15b-SaposinA was subsequently transformed into the *E. coli* strain Rosetta-gami B(DE3). The cells were grown at 37 °C in LB supplemented with 100 μg mL^{-1} ampicillin, 10 μg mL^{-1} tetracycline, 25 μg mL^{-1} chloramphenicol and 50 μg mL^{-1} kanamycin. The cells were induced to an OD600 of 0.6–0.8 with 1 mM isopropyl-beta-D-thiogalactopyranoside (IPTG) at 37 °C for 4 h and were harvested by centrifugation at 40,000 × *g* (Sigma, 12150H rotor) for 30 min at 4 °C. The cell pellet was resuspended in AEX buffer (50 mM Tris-HCl, pH 7.4, 25 mM NaCl) supplemented with 1% protease inhibitor cocktail (APExBIO, K1007) and 5 U ml^{-1} DNase I. The cells were lysed by three passages through a homogenizer (ATS, AH-NANO) at 15000 p.s.i. The lysate was centrifuged at 40,000 × *g* for 30 min. The supernatant was heated at 85 °C for 10 min, followed by an additional centrifugation at 40,000 × *g* for 30 min at 4 °C. The supernatant was loaded onto a HiTrap Q column (GE Healthcare) equilibrated with AEX buffer. The column was washed with 10 column volumes of AEX buffer. The column was eluted with a linear gradient of AEX buffer and elution buffer (20 mM Tris, pH 7.4, 1 M NaCl, 20 mM Tris, pH 7.4). The fractions containing Saposin A were pooled and concentrated to 0.5 ml using an Amicon Ultra15 concentrator (MWCO: 3 kDa). The sample was loaded onto a Superdex 200 column equilibrated with SEC buffer (25 mM HEPES pH 7.5, 300 mM NaCl). The column was eluted with 24 ml of SEC buffer. The fractions containing Saposin A were pooled and concentrated using an Amicon Ultra15 concentrator (MWCO: 3 kDa), flash frozen in liquid nitrogen and stored at -80 °C.

Human Saposin A nanodisc reconstitution was carried out[43] with modifications. In brief, 25 mg of bovine brain lipid extract (B1502; Sigma) was dissolved in 1 mL of chloroform, dried in a vacuum desiccator, resuspended in 1 mL of ddH_2O, sonicated for 30 min, and stored at -20 °C as a stack. For nanodisc reconstitution, 6 mg of Saposin A was mixed with 80 μL of lipid stock (25 mg mL^{-1}), and sodium acetate (50 mM, pH 4.4) was added to the mixture to a final volume of 500 μL. The mixture was incubated at 37 °C for 10 min, 1 mL of SEC buffer (25 mM HEPES, pH 7.5, 300 mM NaCl) was added to the mixture, and the buffer in the mixture was exchanged for SEC buffer using a HiTrap Desalting column. The eluate was pre-formed Saposin A nanodiscs.

Purification of GP64

WT GP64 protein was purified from recombinant baculovirus-infected Sf9 cells. Sf9 cells at a density of 2-3 × 10^6 cells mL^{-1} were infected with the virus expressing CTL2 at a multiplicity of infection of 1.2. The cells were incubated at 27 °C and 120 rpm for 48 h and harvested by centrifugation at 2,000 × *g* for 10 min at room temperature. The cell pellets were stored at -80 °C.

Cell pellets from 1 L of baculovirus-infected cells were resuspended in 50 mL of low-salt buffer (25 mM HEPES, pH 7.5, 10 mM $MgCl_2$, 20 mM KCl, 10% glycerol) and 500 μL of protease inhibitor cocktail (K1007; APExBIO). Cells were homogenized 30 times using a Kimble Dounce homogenizer (D9188; MERCK) and the lysate was subjected to ultracentrifugation using a 70Ti rotor (Beckman Coulter) at 256,630.8 x *g* for 30 min at 4 °C. Pellets were washed twice with 50 mL of high-salt buffer (25 mM HEPES, pH 7.5, 10 mM $MgCl_2$, 20 mM KCl, 1 M NaCl, 10% glycerol, 500 μL of protease inhibitor cocktail) and then resuspended in 50 mL of low-salt buffer supplemented with 2 mg mL^{-1} iodoacetamide. The membrane suspension was incubated for 20 min at 4 °C, and then mixed with 50 mL of solubilization buffer (25 mM HEPES, pH 7.5, 50 mM NaCl, 4% DDM, 0.8% cholesterol hemisuccinate). The mixture was gently stirred for 2 h at 4 °C to solubilize membranes, followed by another round of ultracentrifugation at 433,706 x *g* for 30 min at 4 °C. The supernatant was filtered using a 0.22 μm syringe filter (SLGPR33RB; Millipore) and subsequently loaded onto a 5 mL HisTrap Q HP column (17115301; GE Healthcare) coupled with a Zn^{2+}-charged 1 mL HisTrap Chelating HP column (29051021; GE Healthcare) preequilibrated with equilibrating buffer (25 mM HEPES pH 7.5, 50 mM NaCl, 0.04% DDM, 0.08% cholesterol hemisuccinate). The columns were then dissembled, and the HisTrap HP column was washed with 25 column volumes of washing buffer (25 mM HEPES pH 7.5, 300 mM NaCl, 0.04% DDM, 0.08% cholesterol hemisuccinate). Next, 1 mL of Saposin A nanodiscs was injected onto the HisTrap HP column and incubated for 1 h at 4 °C. GP64 protein was eluted with elution buffer (25 mM HEPES, pH 7.5, 300 mM NaCl, 500 mM imidazole). The eluate was concentrated to 0.5 mL using an Amicon Ultra4 with a 100 kDa molecular weight cut-off (UFC810096; Millipore) and then loaded onto a Superose 6 Increase 10/300GL column (GE Healthcare) preequilibrated with SEC buffer. Fractions containing purified GP64 protein were pooled, concentrated, snap-frozen in liquid nitrogen, and stored at -80 °C.

Cryo-EM data collection

Briefly, 3.0 µL aliquots of purified GP64 protein in Saposin A nanodiscs at a concentration of 0.8 mg mL^{-1} were added to glow-discharged holey gold grids (UltraAuFoil Au R1.2/1.3 300 mesh; Quantifoil Micro Tools GmbH). Excess sample was removed by blotting with filter paper for 3.5 s, after which the sample was rapidly frozen in liquid ethane using a Vitrobot Mark IV (Thermo Fisher Scientific). These specimens were stored in liquid nitrogen until imaging. Zero-energy-loss images of frozen and hydrated grids were automatically captured with a Titan Krios electron microscope at 300 kV using EPU software on a Falcon 4 direct electron detector in counting mode (Thermo Fisher Scientific). A Selectris X energy filter with a slit width of 20 eV was used to exclude inelastically scattered electrons (Thermo Fisher Scientific). Images were saved in EER format, and each movie stack contained 2680 raw images taken at an adjusted magnification of 145,833.3 × (yielding a pixel size of 0.96 Å at the sample level). The dose rate and total dose were ~ 5.34 electrons Å^{-2} s^{-1} (~4.9 electrons pixel^{-1} s^{-1}) and 60.02 electrons Å^{-2}, respectively. The final dataset comprised 4834 movie stacks with defocus values between -1.0 and -2.5 µm.

Cryo-EM image processing

Image processing was performed using RELION v3.1.3 software and wrappers[56,57]. Every EER movie stack was adjusted through gain reference correction, combining every 40 adjacent raw EER images into one averaged movie frame (yielding 67 movie frames), and motion correction with MOTIONCORR2[58]. These motion-corrected movie frames were subsequently combined into averaged micrographs to estimate the contrast transfer function (CTF) using CTFFIND4[59]. Templates for automatic particle picking were derived from (reference-free) two-dimensional classification of a manually selected particle subset. To reduce reference bias, these templates underwent low-pass filtering to 20 Å. Automatic particle picking yielded 2,067,472 particles from 3,724 micrographs, which were extracted using a box size of 360 pixels. After three rounds of 2D classification, a subset of 302,609 particles was selected and extracted again with a box size of 360 pixels.

Subsequent image processing was conducted using CryoSPARC[60]. Particles chosen via 2D classification within RELION were imported into CryoSPARC and underwent an additional round of 2D classification to eliminate any obvious discrepancies, yielding 252,212 particles with randomized orientations. These particles were classified through an ab initio reconstruction procedure using CryoSPARC. The classification included a two-class ab initio reconstruction using an initial minibatch size of 150, a final minibatch size of 600, and a class similarity of 0. This procedure was executed iteratively. The initial and maximum alignment resolution settings were incrementally increased with each classification run (Iteration 1: initial resolution 25 Å, maximum resolution 7 Å; Iteration 2: initial resolution 8 Å, maximum resolution 5 Å). In each iteration, particles yielding a superior 3D volume in the previous round served as the input for the subsequent round. According to this procedure, 104,017 particles contributed to high-quality 3D volumes. These particles were then subjected to nonuniform and local refinements. Next, a 3D variation assay was carried out using 3D Variability software in CryoSPARC with a mask on domain I of GP64. The 3D Variability Display for the dataset generated 20 clusters. Five clusters containing 26,747 particles were combined into particle subset 1, and the remaining 15 clusters containing 70,235 particles were combined into particle subset 2. Particle subset 1 was subjected to nonuniform and local refinements with C3 symmetrical constraints, resulting in a GP64 map-1 with 3-fold symmetry at a resolution of 2.77 Å. Particle subset 2 was subjected to nonuniform refinement and local refinement with C1 symmetrical constraints, yielding asymmetrical GP64 map-2 with a resolution of 2.97 Å (Supplementary Fig. 1a).

All resolution estimations were performed via CryoSPARC using refined half-reconstructions. The criterion for Fourier shell correlation was set at 0.143, and the ResMap wrapper in CryoSPARC was used to calculate local resolution variations[61].

Model building and refinement

For the prefusion state model, two half-maps of GP64 map-1 were used to perform local density sharpening via LocSpiral[62]. The resulting full map with 3-fold symmetry was segmented into three individual maps for protomers. The model sections of domain I and the central helix of domain III from the postfusion structure of GP64 (PDB code: 3DUZ) were fitted into the density map of a GP64 protomer to create an initial model using Chimera[63]. Using the Map to Model software within the Phenix package[64], an automated construction of the GP64 protomer model was created from this initial model, successfully building ~70% of the model. The remaining portion of the model was manually built using Coot[65]. This entire GP64 protomer model was refined via Rosetta[66] and subsequently fitted into the cryo-EM map of the symmetrical GP64 trimer. GP64 map-1 without global B-factor sharpening was used to perform model-based local density sharpening using LocScale[67]. The model of the GP64 trimer was then subjected to real-space refinement against this density-modified map in the Phenix package, resulting in the final prefusion state model.

For the GP64 model in the intermediate-M state, the two half-maps of GP64 map-2 were used to carry out local density sharpening via LocSpiral. The model of the prefusion GP64 trimer was fitted into the density map. Two protomer models of the prefusion GP64 fit well within the map. For the map section corresponding to the third GP64 protomer, both domains I and II of the prefusion GP64 protomer were fitted again separately. To improve the local fit to the density, manual adjustments were made to the model using Coot. The complete model of the asymmetrical GP64 trimer was then subjected to real-space refinement in Phenix.

For the GP64 model in the intermediate-T state, the protomer-M model was fitted into the GP64 map-2 trimer individually using Chimera. The three protomer-M models were subsequently combined to create the model of the intermediate-T trimer.

Any inconsistencies found in the Ramachandran plot were manually corrected in Coot. The stereochemistry of the model was determined using MolProbity[68] (Supplementary Table 2).

cELISA

Cell surface enzyme-linked immunosorbent assay (cELISA) was performed[39]. Briefly, Sf9 cells in 12-well plates (2 × 10^5 cells per well) were transfected with plasmids expressing WT or modified GP64 (2 µg per well). At 36 h post-transfection (p.t.), cells were fixed with 0.5% glutaraldehyde for 10 min, and the cell surface level of GP64 or Myc-tagged GP64 was measured using MAb AcV5 (Catalog no: sc-65499, Santa Cruz Biotechnology, 1:1000 dilution) or anti-Myc MAb 2D5 (Catalog no: ABT2060, Abbkine, 1:1000 dilution), goat anti-mouse IgG conjugated with β-galactosidase (Catalog no: 1030-06, SouthernBiotech, 1:1000 dilution), and the substrate chlorophenol red-D-galactopyranoside (CPRG; Roche Diagnostics GmbH). To assess the low pH-triggered conformational change in cell surface-localized GP64, similarly transfected Sf9 cells (at 36 h p.t.) were incubated in phosphate-buffered saline (PBS) adjusted to different pH values (4.5-7.0) for 20 min, and then fixed with 3.7% paraformaldehyde in PBS (pH 7.0) for 30 min. Following the procedure involving AcV5, GP64 proteins were detected using MAb AcV1 (Catalog no: sc-65498, Santa Cruz Biotechnology, 1:1000 dilution).

Cell-cell syncytium formation, hemifusion, and pore formation assays

Cell-cell syncytium, hemifusion, and pore formation assays were performed[21,39]. Sf9 cells in 12-well plates were transfected with a plasmid expressing WT GP64 (0.005-2 µg per well) or modified GP64 (2 µg per well). At 36 h p.t., for the syncytium formation assay, cells were incubated in PBS at pH 5.0 for 3 min. After washing once with PBS at pH 7.4, cells were maintained in medium at 27 °C for 4 h. Next, cells were fixed with methanol and sequentially stained with 0.1% Eosin Y and 0.1% Methylene Blue[50]. The ratio of nuclei in syncytial masses that contained at least five nuclei in each syncytium to those in a field was calculated and subsequently normalized against those from WT GP64, which was localized to the cell surface at equivalent levels. For hemifusion and pore formation assays, rabbit RBCs were dual-labeled with R18 and calcein-AM (Thermo Fisher Scientific). The transfected Sf9 cells were washed twice with PBS (pH 7.4) and incubated with the labeled RBCs for 20 min. After removing unbound RBCs, cells were washed twice with PBS (pH 7.4), and then incubated in PBS (pH 5.0) for 3 min. After washing once with PBS (pH 7.4), cells were maintained in PBS (pH 7.4) at 27 °C for 20 min. Transfer of fluorescence between RBCs and Sf9 cells was subsequently photographed using an epifluorescence microscope. The efficiency of hemifusion or pore formation was estimated as the ratio of R18-transferred Sf9 cells or calcein-AM-transferred Sf9 cells to RBC-bound Sf9 cells in each field.

Viral infectivity assay

Sf9 cells in 6-well plates (1×10^6 cells per well) were transfected with a bacmid encoding WT or modified GP64 (4 µg per well). At 96 h p.t., supernatants were harvested to infect a new monolayer of Sf9 cells. At 96 h post-infection (p.i.), after removing cells (3,000 × *g*, 10 min), the infectious virus titers were determined via a 50% tissue culture infection dose ($TCID_{50}$) assay. For constructs with significantly lower production of infectious virus, Sf9 cells in 6-well plates were infected with each of the viruses at a MOI of 5 or 0.01. At different time points (24-120 h p.i.), supernatants were collected and infectious virus titers were determined via $TCID_{50}$ assay.

Western blotting

Transfected Sf9 cells (2×10^5 cells) for each construct were lysed in 100 µl RIPA buffer containing protease inhibitor cocktail (Roche Diagnostics GmbH) and then separated into two sets (48 µl per set). After mixing with 12 µl 5× protein loading buffer (with β-mercaptoethanol) or with 12 µl 5× nonreducing loading buffer (without β-mercaptoethanol) (Coolaber), the samples (10 µl of each) were analyzed by 6% (nonreducing) or 10% (reducing) SDS-PAGE. After transferring to PVDF membranes (GVS Filter Technology), proteins were detected using MAb AcV5 (1:2000 dilution), 2D5 (1:2000 dilution), or anti-β-tubulin 3G6 (Catalog no: ABL1030, Abbkine, 1:5000 dilution); alkaline phosphatase-conjugated goat anti-mouse IgG (H + L) secondary antibody (Catalog no: S3721, Promega, 1:10000 dilution); and a BCIP/NBT color development kit (Coolaber).

Reporting summary

Further information on research design is available in the Nature Portfolio Reporting Summary linked to this article.

Data availability

The cryo-EM maps have been deposited in the Electron Microscopy Data Bank (EMDB) under accession codes EMD-39237 (Prefusion GP64) and EMD-39238 (Early intermediate GP64). The atomic coordinates have been deposited in the Protein Data Bank (PDB) under accession codes 8YG6 (Prefusion GP64) and 8YG8 (Early intermediate GP64). In this work, we reference the previously published PDB codes 7XYM (Intermediate DHOV-Gp), 5XEA (Postfusion THOV-Gp), 5XEB (Postfusion DHOV-Gp), 5ZKX (Postfusion BRBV-Gp) and 3DUZ (Postfusion GP64). The source data underlying Fig. 4c, d, Fig. 5a–c, Supplementary Fig. 9, Supplementary Fig. 10 and Supplementary Fig. 11 are provided as a Source Data file. Source data are provided with this paper.

References

1. Podbilewicz, B. Virus and cell fusion mechanisms. *Annu. Rev. Cell Dev. Biol.* **30**, 111–139 (2014).
2. White, J. M., Ward, A. E., Odongo, L. & Tamm, L. K. Viral membrane fusion: a dance between proteins and lipids. *Annu. Rev. Virol.* **10**, 139–161 (2023).
3. Melikyan, G. B. et al. Evidence that the transition of HIV-1 gp41 into a six-helix bundle, not the bundle configuration, induces membrane fusion. *J. Cell Biol.* **151**, 413–423 (2000).
4. Modis, Y., Ogata, S., Clements, D. & Harrison, S. C. Structure of the dengue virus envelope protein after membrane fusion. *Nature* **427**, 313–319 (2004).
5. Roche, S., Rey, F. A., Gaudin, Y. & Bressanelli, S. Structure of the prefusion form of the vesicular stomatitis virus glycoprotein G. *Science* **315**, 843–848 (2007).
6. Roche, S., Bressanelli, S., Rey, F. A. & Gaudin, Y. Crystal structure of the low pH form of the vesicular stomatitis virus glycoprotein G. *Science* **313**, 187–191 (2006).
7. Ozorowski, G. et al. Open and closed structures reveal allostery and pliability in the HIV-1 envelope spike. *Nature* **547**, 360–363 (2017).
8. Chen, J., Skehel, J. J. & Wiley, D. C. N- and C-terminal residues combine in the fusion-pH influenza hemagglutinin HA2 subunit to form an N cap that terminates the triple-stranded coiled coil. *Proc. Natl. Acad. Sci. USA.* **96**, 8967–8972 (1999).
9. Barnard, R. J., Elleder, D. & Young, J. A. Avian sarcoma and leukosis virus-receptor interactions: from classical genetics to novel insights into virus-cell membrane fusion. *Virology* **344**, 25–29 (2006).
10. White, J. M. & Whittaker, G. R. Fusion of enveloped viruses in endosomes. *Traffic* **17**, 593–614 (2016).
11. Jackson, C. B., Farzan, M., Chen, B. & Choe, H. Mechanisms of SARS-CoV-2 entry into cells. *Nat. Rev. Mol. Cell Biol.* **23**, 3–20 (2022).
12. Harrison, J. S. et al. Role of electrostatic repulsion in controlling pH-dependent conformational changes of viral fusion proteins. *Structure* **21**, 1085–1096 (2013).
13. Kampmann, T., Mueller, D. S., Mark, A. E., Young, P. R. & Kobe, B. The role of histidine residues in low-pH-mediated viral membrane fusion. *Structure* **14**, 1481–1487 (2006).
14. Qin, Z. L., Zheng, Y. & Kielian, M. Role of conserved histidine residues in the low-pH dependence of the Semliki Forest virus fusion protein. *J. Gen. Virol.* **83**, 4670–4677 (2009).
15. Fritz, R., Stiasny, K. & Heinz, F. X. Identification of specific histidines as pH sensors in flavivirus membrane fusion. *J. Cell Biol.* **183**, 353–361 (2008).
16. Belot, L. et al. Crystal structure of Mokola virus glycoprotein in its post-fusion conformation. *PLoS Pathog* **16**, e1008383 (2020).
17. Caffrey, M. & Lavie, A. pH-Dependent mechanisms of influenza infection mediated by hemagglutinin. *Front. Mol. Biosci.* **8**, 777095 (2021).
18. Antanasijevic, A., Durst, M. A., Lavie, A. & Caffrey, M. Identification of a pH sensor in Influenza hemagglutinin using X-ray crystallography. *J. Struct. Biol.* **209**, 107412 (2020).
19. Zuzic, L., Marzinek, J. K., Anand, G. S., Warwicker, J. & Bond, P. J. A pH-dependent cluster of charges in a conserved cryptic pocket on flaviviral envelopes. *Elife* **12**, e82447 (2023).
20. Baquero, E., Albertini, A. A. & Gaudin, Y. Recent mechanistic and structural insights on class III viral fusion glycoproteins. *Curr. Opin. Struct. Biol.* **33**, 52–60 (2015).

21. Kadlec, J., Loureiro, S., Abrescia, N. G., Stuart, D. I. & Jones, I. M. The postfusion structure of baculovirus gp64 supports a unified view of viral fusion machines. *Nat. Struct. Mol. Biol.* **15**, 1024–1030 (2008).
22. Matsuura, H., Kirschner, A. N., Longnecker, R. & Jardetzky, T. S. Crystal structure of the epstein- barr virus (EBV) glycoprotein H/ glycoprotein L (gH/gL) complex. *Proc. Natl Acad. Sci. USA* **107**, 22641–22646 (2010).
23. Heldwein, E. E. et al. Crystal structure of glycoprotein B from herpes simplex virus 1. *Science* **313**, 217–220 (2006).
24. Burke, H. G. & Heldwein, E. E. Crystal structure of the human cytomegalovirus glycoprotein B. *PLoS Pathog* **11**, e1005227 (2015).
25. Baquero, E. et al. Structure of the low pH conformation of Chandipura virus G reveals important features in the evolution of the vesiculovirus glycoprotein. *PLoS Pathog* **11**, e1004756 (2015).
26. Bai, C. et al. Postfusion structure of human-infecting bourbon virus envelope glycoprotein. *J. Struct. Biol.* **208**, 99–106 (2019).
27. Peng, R. et al. Structures of human-infecting thogotovirus fusogens support a common ancestor with insect baculovirus. *Proc. Natl. Acad. Sci. USA.* **114**, E8905–E8912 (2017).
28. Baquero, E. et al. Structural intermediates in the fusion-associated transition of vesiculovirus glycoprotein. *EMBO J.* **36**, 679–692 (2017).
29. Yang, F. et al. Structural analysis of rabies virus glycoprotein reveals pH-dependent conformational changes and interactions with a neutralizing antibody. *Cell Host Microbe.* **27**, 441–453.e7 (2020).
30. Connolly, S. A., Jardetzky, T. S. & Longnecker, R. The structural basis of herpesvirus entry. *Nat. Rev. Microbiol.* **19**, 110–121 (2021).
31. Sardar, A., Dewangan, N., Panda, B., Bhowmick, D. & Tarafdar, P. K. Lipid and lipidation in membrane fusion. *J. Membr. Biol.* **255**, 691–703 (2022).
32. Beilstein, F. et al. Identification of a pH-sensitive switch in VSV-G and a crystal structure of the G pre-fusion state highlight the VSV-G structural transition pathway. *Cell Rep.* **32**, 108042 (2020).
33. Ferlin, A., Raux, H., Baquero, E., Lepault, J. & Gaudin, Y. Characterization of pH-sensitive molecular switches that trigger the structural transition of vesicular stomatitis virus glycoprotein from the postfusion state toward the prefusion state. *J. Virol.* **88**, 13396–13409 (2014).
34. Liu, Y. et al. Prefusion structure of human cytomegalovirus glycoprotein B and structural basis for membrane fusion. *Sci. Adv.* **7**, eabf3178 (2021).
35. Vollmer, B. et al. The prefusion structure of herpes simplex virus glycoprotein B. *Sci. Adv.* **6**, eabc1726 (2020).
36. Vollmer, B. & Grünewald, K. Herpesvirus membrane fusion—a team effort. *Curr. Opin. Struct. Biol.* **62**, 112–120 (2020).
37. Cooper, R. S., Georgieva, E. R., Borbat, P. P., Freed, J. H. & Heldwein, E. E. Structural basis for membrane anchoring and fusion regulation of the herpes simplex virus fusogen gB. *Nat. Struct. Mol. Biol.* **25**, 416–424 (2018).
38. Blissard, G. W. & Wenz, J. R. Baculovirus GP64 envelope glycoprotein is sufficient to mediate pH-dependent membrane fusion. *J. Virol.* **66**, 6829–6835 (1992).
39. Li, Z. & Blissard, G. W. Autographa Californica multiple nucleopolyhedrovirus GP64 protein: roles of histidine residues in triggering membrane fusion and fusion pore expansion. *J. Virol.* **85**, 12492–12504 (2011).
40. Blissard, G. W. & Theilmann, D. A. Baculovirus entry and egress from insect cells. *Annu. Rev. Virol.* **5**, 113–139 (2018).
41. Hefferon, K. L., Oomens, A. G., Monsma, S. A., Finnerty, C. M. & Blissard, G. W. Host cell receptor binding by baculovirus GP64 and kinetics of virion entry. *Virology* **258**, 455–468 (1999).
42. Zhou, J. & Blissard, G. W. Identification of a GP64 subdomain involved in receptor binding by budded virions of the baculovirus autographica californica multicapsid nucleopolyhedrovirus. *J. Virol.* **82**, 4449–4460 (2008).
43. Du, D. et al. Interactions of a bacterial RND transporter with a transmembrane small protein in a lipid environment. *Structure* **28**, 625–634.e6 (2020).
44. Frauenfeld, J. et al. A saposin-lipoprotein nanoparticle system for membrane proteins. *Nat. Methods* **13**, 345–351 (2016).
45. Jarvis, D. L., Wills, L., Burow, G. & Bohlmeyer, D. A. Mutational analysis of the N-linked glycans on autographa californica nucleopolyhedrovirus gp64. *J. Virol.* **72**, 9459–9469 (1998).
46. Dong, S. & Blissard, G. W. Functional analysis of the autographa californica multiple nucleopolyhedrovirus GP64 terminal fusion loops and interactions with membranes. *J. Virol.* **86**, 9617–9628 (2012).
47. Li, Z. & Blissard, G. W. Baculovirus GP64 disulfide bonds: the intermolecular disulfide bond of autographa californica multicapsid nucleopolyhedrovirus GP64 is not essential for membrane fusion and virion budding. *J. Virol.* **84**, 8584–8595 (2010).
48. Zhou, J. & Blissard, G. W. Mapping the conformational epitope of a neutralizing antibody (AcV1) directed against the AcMNPV GP64 protein. *Virology* **352**, 427–437 (2006).
49. Hohmann, A. W. & Faulkner, P. Monoclonal antibodies to baculovirus structural proteins determination of specificities by Western blot analysis. *Virology* **125**, 432–444 (1983).
50. Yu, Q., Blissard, G. W., Liu, T. X. & Li, Z. Autographa californica multiple nucleopolyhedrovirus GP64 protein: Analysis of domain I and V amino acid interactions and membrane fusion activity. *Virology* **488**, 259–270 (2016).
51. Li, Z. & Blissard, G. W. The pre-transmembrane domain of the autographa californica multicapsid nucleopolyhedrovirus GP64 protein is critical for membrane fusion and virus infectivity. *J. Virol.* **83**, 10993–11004 (2009).
52. Li, Z. & Blissard, G. W. The autographa californica multicapsid nucleopolyhedrovirus GP64 protein: analysis of transmembrane domain length and sequence requirements. *J. Virol.* **83**, 4447–4461 (2009).
53. Baquero, E. et al. Intermediate conformations during viral fusion glycoprotein structural transition. *Curr. Opin Virol.* **3**, 143–150 (2013).
54. Connolly, S. A. & Longnecker, R. Residues within the C-terminal arm of the herpes simplex virus 1 glycoprotein B ectodomain contribute to its refolding during the fusion step of virus entry. *J. Virol.* **86**, 6386–6393 (2012).
55. Hu, L. et al. The major hurdle for effective baculovirus transduction into mammalian cells is passing early endosomes. *J. Virol.* **93**, e00709–e00719 (2019).
56. Scheres, S. H. RELION: implementation of a Bayesian approach to cryo-EM structure determination. *J. Struct. Biol.* **180**, 519–530 (2012).
57. Zivanov, J. et al. New tools for automated high-resolution cryo-EM structure determination in RELION-3. *Elife* **7**, e42166 (2018).
58. Li, X. et al. Electron counting and beam-induced motion correction enable near-atomic-resolution single-particle cryo-EM. *Nat. Methods* **10**, 584–590 (2013).
59. Rohou, A. & Grigorieff, N. CTFFIND4: Fast and accurate defocus estimation from electron micrographs. *J. Struct. Biol.* **192**, 216–221 (2015).
60. Punjani, A., Rubinstein, J. L., Fleet, D. J. & Brubaker, M. A. cryoSPARC: algorithms for rapid unsupervised cryo-EM structure determination. *Nat. Methods* **14**, 290–296 (2017).
61. Kucukelbir, A., Sigworth, F. J. & Tagare, H. D. Quantifying the local resolution of cryo-EM density maps. *Nat. Methods* **11**, 63–65 (2014).
62. Kaur, S. et al. Local computational methods to improve the interpretability and analysis of cryo-EM maps. *Nat. Commun.* **12**, 1240 (2021).

63. Pettersen, E. F. et al. UCSF chimera-a visualization system for exploratory research and analysis. *J. Comput. Chem.* **25**, 1605–1612 (2004).
64. Liebschner, D. et al. Macromolecular structure determination using X-rays, neutrons and electrons: recent developments in Phenix. *Acta. Crystallogr. D* **75**, 861–877 (2019).
65. Emsley, P., Lohkamp, B., Scott, W. G. & Cowtan, K. Features and development of coot. *Acta Crystallogr. D* **66**, 486–501 (2010).
66. Wang, R. Y. et al. Automated structure refinement of macromolecular assemblies from cryo-EM maps using Rosetta. *Elife* **5**, e17219 (2016).
67. Jakobi, A. J., Wilmanns, M. & Sachse, C. Model-based local density sharpening of cryo-EM maps. *eLife* **6**, e27131 (2017).
68. Williams, C. J. et al. MolProbity: More and better reference data for improved all-atom structure validation. *Protein Sci.* **27**, 293–315 (2018).

Acknowledgements

This work was supported by the National Natural Science Foundation of China (31971133 to D.D.; 32172485 to Z.L.) and the Science and Technology Commission of Shanghai Municipality (19PJ1407900, 19JC1414000 and 22WZ2504100 to D.D.). Cryo-EM data were collected at the Bio-Electron Microscopy Facility of ShanghaiTech University with the assistance of Q. Sun, D. Liu, Z. Zhang, L. Wang and Y. Yang. We thank the Molecular Imaging Core Facility, the Molecular and Cell Biology Core Facility, and the Multi-Omics Core Facility at the School of Life Science and Technology for providing technical support.

Author contributions

J.G. and S.L. purified the GP64, prepared cryo-EM samples, collected cryo-EM data, determined structures, performed model building and refinement and prepared figures for the manuscript; H.Z., W.S., Z.Z., T.M., and X.G. optimized in-column Saposin A nanodisc methods, and assisted the collection of cryo-EM data; L.B. and N.J. constructed the modified GP64 and performed membrane fusion assay; Z.L. performed cELISA and virus infection assay; D.D. and Z.L. conceived the projects; D.D. and Z.L. designed and supervised all experiments; D.D., Z.L. and Y.C. wrote the manuscript. All the authors contributed to the data interpretation and manuscript preparation.

Competing interests

The authors declare no competing interests.

Additional information

Supplementary information The online version contains supplementary material available at https://doi.org/10.1038/s41467-024-51799-4.

Correspondence and requests for materials should be addressed to Zhaofei Li or Dijun Du.

Peer review information *Nature Communications* thanks the anonymous reviewers for their contribution to the peer review of this work. A peer review file is available.